AGU PUBLICATIONS

JGR

Journal of Geophysical Research: Space Physics

RESEARCH ARTICLE

10.1002/2013JA019547

Key Points:
- RAX provides highest-resolution measurements of auroral FAI
- Magnetic aspect sensitivity of submeter FAI is stronger than thought
- Submeter waves may not significantly contribute to wave heating

Correspondence to:
H. Bahcivan,
hasan.bahcivan@sri.com

Citation:
Bahcivan, H., J. W. Cutler, J. C. Springmann, R. Doe, and M. J. Nicolls (2014), Magnetic aspect sensitivity of high-latitude *E* region irregularities measured by the RAX-2 CubeSat, *J. Geophys. Res. Space Physics*, *119*, 1233–1249, doi:10.1002/2013JA019547.

Received 15 OCT 2013
Accepted 20 DEC 2013
Accepted article online 14 JAN 2014
Published online 12 FEB 2014

Magnetic aspect sensitivity of high-latitude *E* region irregularities measured by the RAX-2 CubeSat

H. Bahcivan[1], J. W. Cutler[2], J. C. Springmann[2], R. Doe[1], and M. J. Nicolls[1]

[1]Center for Geospace Studies, SRI International, Menlo Park, California, USA, [2]Department of Aerospace Engineering, University of Michigan, Ann Arbor, Michigan, USA

Abstract The second Radio Aurora Explorer (RAX-2) satellite has completed more than 30 conjunction experiments with the Advanced Modular Incoherent Scatter Radar chain of incoherent scatter radars in Alaska and Resolute Bay, Canada. Coherent radar echoing occurred during four of the passes: three when *E* region electron drifts exceeded the ion acoustic speed threshold and one during HF heating of the ionosphere by the High Frequency Active Auroral Research Program heater. In this paper, we present the results for the first three passes associated with backscatter from natural irregularities. We analyze, in detail, the largest drift case because the plasma turbulence was the most intense and because the corresponding ground-to-space bistatic scattering geometry was the most favorable for magnetic aspect sensitivity analysis. A set of data analysis procedures including interference removal, autocorrelation analysis, and the application of a radar beam deconvolution algorithm mapped the distribution of *E* region backscatter with 3 km resolution in altitude and ~0.1° in magnetic aspect angle. To our knowledge, these are the highest resolution altitude-resolved magnetic aspect sensitivity measurements made at UHF frequencies in the auroral region. In this paper, we show that despite the large electron drift speed of ~1500 m/s, the magnetic aspect sensitivity of submeter scale irregularities is much higher than previously reported. The root-mean-square of the aspect angle distribution varied monotonically between 0.5° and 0.1° for the altitude range 100–110 km. Findings from this single but compelling event suggest that submeter scale waves propagating at larger angles from the main $\mathbf{E} \times \mathbf{B}$ flow direction (secondary waves) have parallel electric fields that are too small to contribute to *E* region electron heating. It is possible that anomalous electron heating in the auroral electrojet can be explained by (a) the dynamics of those submeter scale waves propagating in the $\mathbf{E} \times \mathbf{B}$ direction (primary waves) or (b) the dynamics of longer wavelengths.

1. Introduction

The terminology field-aligned irregularities (FAI) refers to electron density structures that are strongly aligned with the geomagnetic field, **B**. The principal reason for the alignment is the large ratio of parallel (in the direction of **B**) and Pedersen ionospheric conductivities (σ_0/σ_P). A small misalignment of FAI from **B** results in wave-generated parallel electric fields ($\delta E_{||}$) that dissipate significantly larger energy per mV/m than perpendicular electric fields. The objective of this paper is to assess the magnetic field alignment of auroral *E* region FAI as a function of altitude and discuss its implications on wave heating of the background plasma.

Various plasma instabilities produce FAI in the auroral *E* region. The most well-known affecting the energetics of the auroral ionosphere [*Dimant and Oppenheim*, 2011a, 2011b] is the Farley-Buneman instability [*Farley*, 1963; *Buneman*, 1963]. The generated waves have been held responsible for electron heating [*Schlegel and St.-Maurice*, 1981; *St.-Maurice et al.*, 1981; *Foster and Erickson*, 2000; *Bahcivan*, 2007] with the electron temperatures rising from 300 K to as high as 4000 K as the background electric field increases. Considerable effort has been made in the last decade to analytically and numerically model the heating process [*Milikh and Dimant*, 2003a, 2003b; *Bahcivan et al.*, 2006; *Oppenheim et al.*, 2008; *Oppenheim and Dimant*, 2013]. However, although the models reproduce the enhanced electron temperatures well, a basic assumption or prediction underlying the models relating to the magnetic field alignment of FAI has not been verified. Determination of magnetic aspect sensitivity, from which RMS $E_{||}$ can be estimated, is critical not only for quantifying electron heating and subsequent changes in the plasma chemistry but also for quantifying total Joule heating rates in the ionosphere due to solar and magnetospheric forcing.

A large literature exists on ground-based radar measurements of magnetic aspect sensitivity of *E* region irregularities [e.g., *Tsunoda et al.*, 1974; *Schlegel and Moorcroft*, 1989; *Moorcroft and Schlegel*, 1990; *Foster et al.*, 1992; *Hall and Moorcroft*, 1992; *Moorcroft*, 1996; *Jackel et al.*, 1997]. However, it has not been possible to fully verify the assumptions made by the theoretical models we have just mentioned because (1) the ground-based radars do not have the altitude resolution to resolve the most heated layer of the electrojet near the altitude of 110 km and (2) they do not have aspect angle resolution to resolve the aspect sensitivities to a fraction of a degree. The main reason for the poor resolution is because ground-based radars in the high latitudes must be pointed to very low elevations to meet the perpendicularity condition. And, at low elevations, radar beam at the altitude of scattering spans the entire *E* region, if not wider, which makes it difficult to resolve an electrojet irregularity layer that is only several kilometers thick in altitude. Besides, for a given FAI occurrence, the driving electric field may not be fully characterized, unless an incoherent scatter radar is nearby and operating simultaneously. Generally speaking, magnetic aspect sensitivity of auroral *E* region scatter has been described in terms of power drop per degree away from perpendicularity, e.g., a consensus measurement is that power drops by 10 dB per degree in the first few degrees off perpendicularity. Note that (1) the power drop rate within the first fractions of a degree, (2) the specific altitude of the observation, and (3) the driving electric field are not specified in this description, which are essential to fully characterize *E* region plasma waves. Herein, we present a unique radar observation that produced a data set that contains these three pieces of information.

The Radio Aurora Explorer (RAX) mission [*Bahcivan and Cutler*, 2012] was designed as a ground-to-space bistatic radar experiment to overcome aforementioned limitations of ground-based radars: an experiment is carried out using a powerful and narrow beam width transmitter on the ground, i.e., an incoherent scatter radar (ISR), and an orbiting UHF radar receiver that captures the ISR's direct pulse and the coherent echoes in space. If a short ISR pulse baud of 10 μs is used, the scattering region, which is confined to the inside of the ∼1° wide ISR beam width, is only several kms in extent inside the *E* region. Moreover, as discussed in detail in the text, the receiver's orbital motion allows us to deconvolve the ∼1° radar beam from the measurements, allowing aspect sensitivity determination to a fraction of a degree. Furthermore, a RAX experiment affords the opportunity to measure vector electric fields and plasma densities probed simultaneously by the incoherent scatter radar, enabling the fine quantification of the ionospheric drivers that lead to plasma instabilities. Such altitude-resolved aspect sensitivity measurements, as a function of the driving electric field, are necessary to meaningfully characterize the altitude-dependent properties of *E* region plasma waves.

RAX is the first CubeSat mission funded by the NSF CubeSat-based Space Weather program [*Moretto*, 2008]. The mission science and radar system were described in detail in *Bahcivan et al.* [2009] and *Bahcivan and Cutler* [2012]. The mission has been jointly conducted by SRI International and the University of Michigan. The RAX-1 satellite was launched in December 2010; however, the spacecraft operations were terminated after a few months due to a solar panel failure. The RAX-2 satellite was launched in October 2011 from Vandenberg Air Force Base to a 104° inclination, elliptical orbit (400-820 km). The launch was provided by NASA's Educational Launch of Nanosatellites (ELaNa) program. After 1.5 years of successful operation, RAX-2 was also terminated in June 2013.

As of June 2013, RAX-2 completed more than 30 experiments with the Advanced Modular Incoherent Scatter Radar (AMISR) chain of ISRs in Poker Flat, Alaska, and Resolute Bay, Canada, as well as the small AMISR system in Gakona, Alaska. Coherent radar echoing occurred during four of the 30 passes: three with *F* region ion drifts reaching ∼700, 1000, and 1600 m/s, and one during artificial HF heating of the ionosphere by the HAARP heater. In this paper, we present the results from the three natural irregularity cases and analyze in further detail the high-resolution magnetic aspect sensitivity data from the largest drift case that occurred during the magnetic storm of 8 March 2012, hereinafter referred to as EXPT1017.

2. Observations

2.1. EXPT1017, 8 March 2012

Figure 1 shows the loci-of-perpendicularity for the satellite trajectory during EXPT1017, with the satellite path shown by the dashed black line. The satellite was descending in latitude (flying equatorward). Details of the ground-to-space bistatic scattering geometry can be seen in *Bahcivan and Cutler* [2012], including the altitude and aspect angle radar ambiguity functions for several crossings of the loci-of-perpendicularity. The Poker Flat Incoherent Scatter Radar (PFISR) made incoherent radar measurements of the ionospheric plasma parameters. The $\mathbf{E} \times \mathbf{B}$ drift vector shown in Figure 1 represents the average of *F* region ion drift

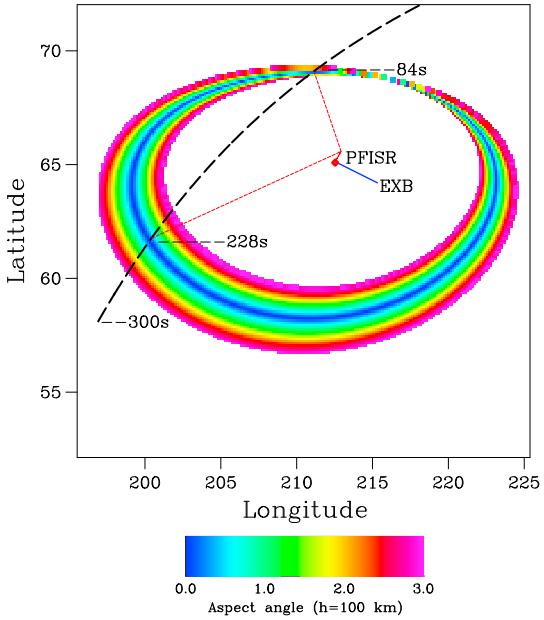

Figure 1. EXPT1017 geometry showing the loci-of-perpendicularity at the spacecraft altitude (colored rings), the ground projections of the spacecraft trajectory (dashed line), and the incoming and scattered radar wave direction (thin red lines). The blue vector shows the ground projection of the $\mathbf{E} \times \mathbf{B}$ drift vector during the pass. The aspect angle scale is in degrees.

velocity measurements between the magnetic latitudes of 67–68°. The UHF payload radar receiver on RAX-2 was turned on for 300 s over the experimental zone, starting at 17:10:24 UT on 8 March 2012. The receiver collected 14 bit I and Q samples at a rate of 1 MHz each. Meanwhile, PFISR transmitted pulses in six look directions. The beam dedicated to spacecraft reception of backscatter was pointed at 20.8° east of north and at 58.0° elevation, sending 100 μs uncoded pulses at 449 MHz every 10 ms. Halfway between the 100 μs pulses, 480 μs long pulses were transmitted at 449.5 MHz to measure the background ionospheric parameters using the incoherent scatter measurement technique. In the several weeks following this experiment, we downloaded the raw I and Q data collected near the two crossings of the loci-of-perpendicularity at times 84 s and 228 s after the on board radar data acquisition began (see Figure 1). A total of 75 s of raw data was downloaded for this pass alone. Due to the low telemetry rate, the download took several months.

Figure 2 shows the range-time-intensity (RTI) plot for this experiment. The abscissa in this figure and the other RTI plots throughout this paper are given in terms of time after the start of the data acquisition. An onboard timer is programmed to start the data acquisition at the time indicated at the title of the RTI plot. However, the onboard clock can be off by a number of seconds. The collected data is postsynchronized to a fraction of a second, as described below. According to the satellite ephemeris, RAX-2 went through the second crossing of the loci-of-perpendicularity for the altitudes of 300 (*F* region), 200, and 100 km (*E* region) at times 175, 205, and 235 s after 17:10:24 UT, respectively. The only echoes detected arrived from the *E* region. The observed echoing time range was between the times of 195 and 245 s after 17:10:24 UT for the second crossing. During this pass, the *F* region ion drift

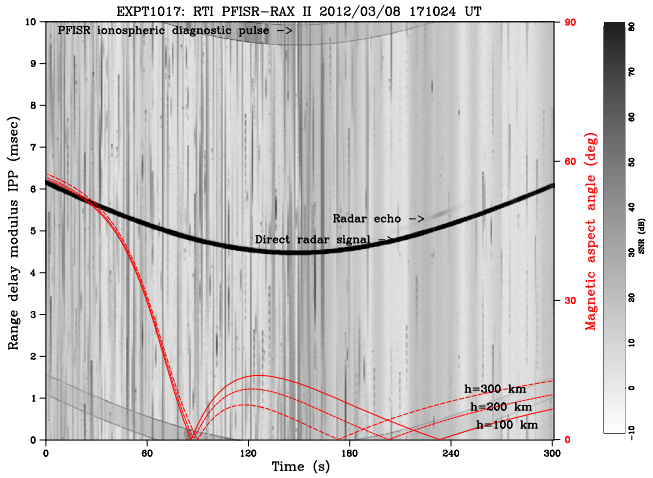

Figure 2. Range-time-intensity plot for the 300 s RAX-PFISR conjunction experiment (EXPT1017). The abscissa is in seconds after the start of the data acquisition. The thick black trace is the 100 μs PFISR direct signal. The wider (in the direction of the ordinate) faint trace is due to 480 μs long PFISR diagnostic pulses at 449.5 MHz. The aspect angles as a function of time corresponding to the irregularity altitudes of 100, 200, and 300 km are shown by the solid, short-dashed, and long-dashed red lines, respectively. Note that the ordinate for these lines is the right-hand *y* axis. FAI backscatter from these altitudes are expected when the aspect angle dips near zero. The faint trace near 235 s arriving shortly (~330 μs) after the direct signal is the *E* region echo.

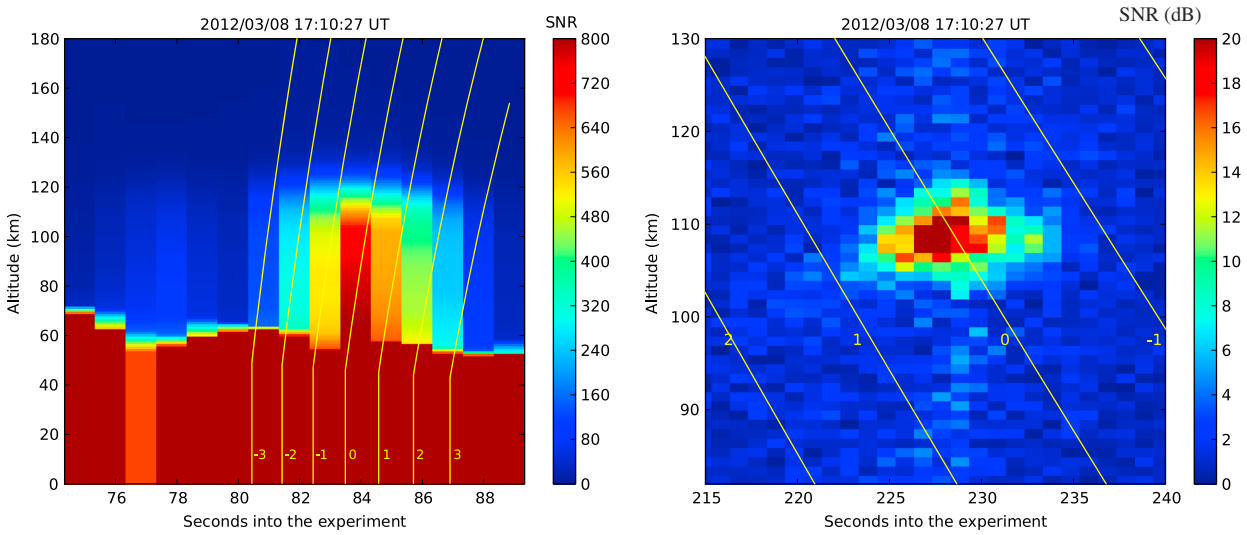

Figure 3. Radar echoes mapped to altitude and aspect angle/time coordinates for the (left) first and (right) second crossing of the loci of perpendicularity. The yellow lines are the aspect angle contours separated by 1° each. The intensity scale is linear.

magnitude measured by PFISR (based on the 480 μs diagnostic pulses transmitted within the 300 s window) was 1543 ± 150 m/s. The corresponding *E* region $\mathbf{E} \times \mathbf{B}$ drift significantly exceeds the ion acoustic threshold for the Farley-Buneman instability [*Farley*, 1963; *Buneman*, 1963]. The projection of the $\mathbf{E} \times \mathbf{B}$ drift on the bistatic radar Bragg wave vector (for the second crossing of the loci-of-perpendicularity) was 900 ± 84 m/s.

The peak of the scattering during the first crossing corresponds to an effective bistatic Bragg wavelength of 2.42 m and an effective bistatic radar frequency of 62 MHz. During the second crossing, which is of main interest here, the Bragg wavelength and radar frequency are 0.53 m and 283 MHz, respectively. Therefore, although the transmitter operates in the UHF band, the bistatic radar effectively operates in the VHF band for this particular geometry. As we show later in the paper, the echoing from the first crossing cannot be resolved well because of the poor range ambiguity function, but it is clearly centered at *E* region altitudes. For the second crossing, echoing occurred ~330 ms after the arrival of the direct pulse, corresponding to an *E* region altitude of ~109 km.

Assuming coherent echoes originate inside the narrow (~1° full width at half power) ISR beam, we calculated the echo altitudes and magnetic aspect angles from the echo delays, i.e., the time elapsed since the arrival of the direct pulse. We mapped the echo intensity as a function of delay to altitude and contours of magnetic aspect angle. The results for the two crossings of the loci-of-perpendicularity are shown in Figure 3. The left-hand-side (LHS) is the first crossing and the right-hand side (RHS) is the second. Note that accurate timing of radar data acquisition is critical for accurate mapping of the echoes aspect angles. For the first crossing, 1 s clock error translates to ~ 1.05° aspect angle change. For the second crossing, 1 s clock error corresponds to ~ 0.12° error in aspect angle. Although GPS was not operated, we were able to determine the onboard clock error to a precision of ~20 ms using direct PFISR pulses. This ensured that any aspect angle bias due to the clock error is negligible, i.e., < 0.002°.

The determination of the clock error was done as follows: The times of PFISR pulse transmissions are known to GPS accuracy. The arrival times of direct PFISR pulses (from the PFISR antenna sidelobes) at the spacecraft are time-tagged via the timestamping of 1 MHz I and Q samples. The arrival time of a PFISR direct pulse is determined from the rising edge to a precision of several μs. Then, the expected (theoretical) arrival time of the direct pulse is calculated from the satellite position and the fixed PFISR position on the ground. The onboard clock error is estimated by matching the measured arrival times with the theoretical arrival times using a linear (offset and constant drift) clock model. We estimated that the clock was ahead by 4.50 ± 0.02 s. As seen in Figure 3, after correcting the time of the data, we find that peak of the echoing occurred when the scattering was perpendicular to *B*, within a fraction of a degree.

The second crossing of the loci-of-perpendicularity provided the best aspect angle resolution (see Figure 3, right). The spacecraft took ~8 s to travel across contours spaced 1° apart. This is also seen in Figure 1 where

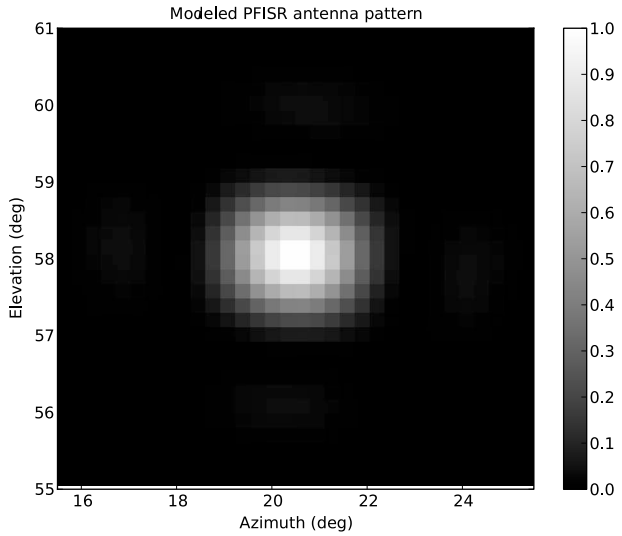

Figure 4. The modeled PFISR antenna pattern for the boresight pointed at azimuth (AZ), elevation (el): (20.8°, 58.0°). The scale is linear. A total of 1024 infinitely narrow beams compose the model. A forward scattering model is constructed to simultaneously illuminate the ionosphere using these beams and to apply proper propagation delays to reproduce the image in Figure 3.

the loci-of-perpendicularity segment (between −3° and 3°) of the spacecraft trajectory is much longer for the second crossing than the first. Note that the spacecraft is descending in latitude.

Figure 3 (left) shows that the 3 dB full width of the aspect angle distribution between the altitudes of 105 and 115 km is ≤0.5°. As we discuss below, this spread is in large part due to the finite beam width of PFISR (~1°). If the irregularities were perfectly field-aligned, the width of the distribution would be approximately half of the beam width, ~0.5°. This can be seen by picturing PFISR's beam as consisting of two infinitely narrow beams that are 1° apart. Since the spacecraft-to-irregularity distance is an order of magnitude larger than the PFISR-to-irregularity distance, the corresponding Bragg wave vectors of the two infinitely narrow beams are about 0.5° apart. Since the measured width of the distribution (Figure 3, right) is also ~0.5°, this implies that the width of the echoing region is mainly a result of the convolution of the beam with a highly field-aligned target. Therefore, to quantify the distribution to a better precision, we have to deconvolve the radar beam from the measurements.

The first step to the deconvolution is to model the PFISR antenna radiation pattern using the known spatial and phase configuration of all the 4096 transmitter elements that contribute to the boresight direction (20.8° azimuth and 58° elevation). A fraction (<25%) of the transmitter elements were not radiating; however, we do not anticipate a significant effect in our deconvolution results below. Figure 4 shows the modeled beam pattern which has been pixelated as 1024 beams spread around the radar boresight. Next, a forward scattering model is constructed where the intensity of each of the 1024 beam is proportional to the gain pattern at the corresponding azimuth/elevation offset from boresight and where the proper propagation delays are applied to each beam.

The inputs to the forward scattering model are E region altitude [h] profiles of (1) backscatter intensity $I[h]$, (2) aspect sensitivity $\Delta\theta[h]$, and (3) mean aspect angle $\theta_m[h]$. These profiles spanned the altitudes of 81–130 km with 1 km steps (50 points each profile). Note that we assume the ionosphere was horizontally homogeneous and that the echoes originating inside the radar beam were driven by the same electric field. As we reported in *Bahcivan et al.* [2012], the electric field as measured using six PFISR beams was fairly uniform throughout the PFISR imaging area.

The altitude profiles were initialized as follows: $I[h]$ was initialized as a Gaussian profile centered near 110 km; $\Delta\theta[h]$ was initialized as monotonically decreasing with increasing altitude, tapered at 0.5° for ≤100 km and 0.05° at ≥115 km; $\theta_m[h]$ was initialized at 0° at every altitude. Then, we let the profiles float freely and applied random perturbations and a smoothing filter for each altitude between 100 and 115 km to seek the profiles whose forward model matched the measured image based on the least mean squares (LMS) criterion. Further details on the forward modeling are given in Appendix A.

Figure 5 shows the best fit output of the forward model. The output agrees visually well with the measurement shown in Figure 3. The root-mean-square error of the entire image is at 4% of the peak power in the image, which is near the estimated (normalized) noise floor of 0.039. The best fit profiles and the error bars are shown in Figure 6. The error bars are computed from the diagonal elements of the covariance matrix $C = (J^T J)^{-1}$ where J is the Jacobian matrix of the function minimized (see Appendix A). The $I[h]$ profile seen on the Figure 6 (left) shows that the echoes are centered at the altitude of 109 km with the 3 dB fall off

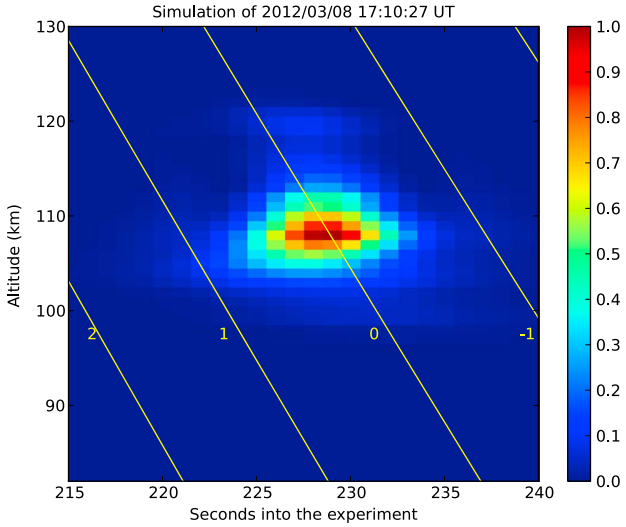

Figure 5. Output of the best fit forward model. The peak intensities of both the data image and the model image are normalized to unity. Compare to Figure 3. The best fit *E* region profiles are shown in Figure 6. The intensity scale is linear.

points located at 106 and 112 km. The aspect sensitivity profile seen in Figure 6 (middle) shows that the RMS spread of the aspect angle distribution is 0.05° ± 0.05° at 115 km, 0.15° ± 0.05° at 110 km, and 0.35° ± 0.10° at 105 km. The $\theta_m[h]$ profile seen on Figure 6 (right) shows that the mean aspect angle gradually changes from near 0° at 115 km to 0.4° at 105 km altitude. As we discuss below, the variation in the mean aspect angle may be accounted for by the perturbation of the background geomagnetic field by the electrojet current.

Although there are numerous input parameters to the forward model, the best fit profiles are primarily determined by a smaller set of parameters around the echo altitude range of 106–112 km, which produced the largest radar returns. Various initializations converged on similar solutions, i.e., a peak scattering location around 109 km, 0.1–0.2° aspect width at 109 km, monotonically increasing to 0.4–0.5° at 105 km and below. See Appendix A for details on this sensitivity study. Because of the lack of backscatter signals, the estimates for altitudes below 105 km and above 112 km are largely driven by the smoothness criteria, and the results have a correspondingly large error.

As we discuss below, based on the linear theory as well as the models of wave heating, the common expectation is that the aspect angle spread should have been more than 1° at the altitude of 110 km, especially for an $\mathbf{E} \times \mathbf{B}$ electron drift of more than 1500 m/s [*Oppenheim and Dimant*, 2013]. The altitude-aspect angle image corresponding to this expectation is of interest here, in particular, due to a possible concern that there may be too many input parameters into the fitter and that the final solution may represent only one of many arbitrary solutions. We therefore contrast the measured image with the expected image by computing (via the forward scattering model) the image the satellite would have recorded if we increased the best fit aspect angle width profile ($\Delta\theta[h]$) by 1° at every altitude. We kept the best fit intensity and mean aspect angle profiles the same. The results are shown in Figure 7. The distribution of echoes in altitude does not noticeably change. However, the aspect angle spread at the altitude of 110 km is now near 2°, as expected from the convolution of a 1° beam with scattering from a target whose aspect angle spreads is 1°. Quite clearly, Figure 7 is very different (much broader) than the measured image (Figure 3, right). This suggests

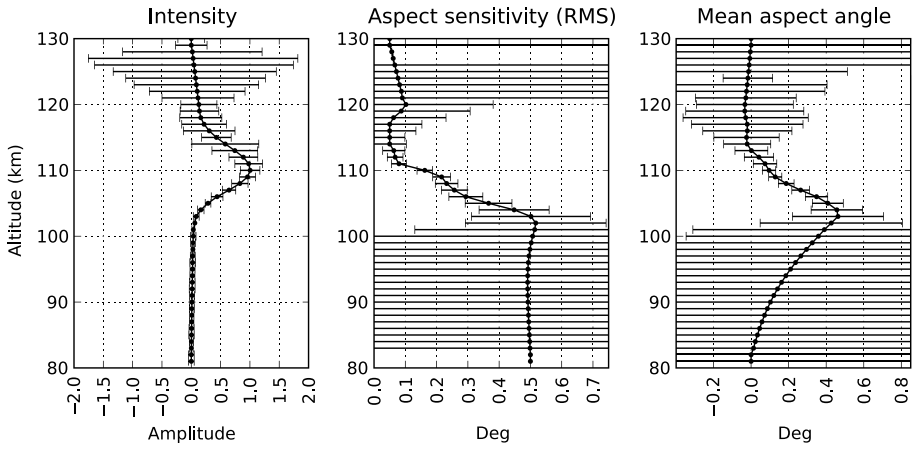

Figure 6. (left) *E* region scattering intensity, (middle) aspect sensitivity, and (right) mean aspect angle profiles that produced the forward model image (Figure 5) that best fitted the measured radar image shown in Figure 3 (right).

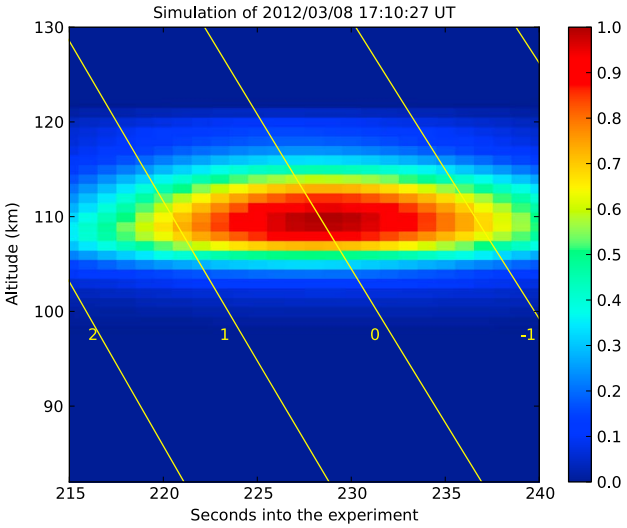

Figure 7. Simulation of scattering for the same *E* region best fit altitude profiles (Figure 6), except that the RMS aspect angle profile is increased by 1° throughout 80–130 km. (The intensity scale is linear).

that it is unlikely that a $\Delta\theta[h]$ profile with a value near 1° would be a solution. This means the magnetic aspect sensitivity of FAI at 110 km should have been much smaller than 1° to produce the image on the RHS of Figure 3.

It would have been very helpful to have comparable resolution aspect sensitivity data from the first crossing of EXPT1017 (Figure 3, left) to compare to the second crossing. However, this is not possible because the scattering geometry results in very poor aspect angle resolution (1°), about 8 times lower than the second crossing and extremely poor altitude resolution (20–40 km). As can be seen from the loci-of-perpendicularity in Figure 1, the spacecraft moves much more rapidly (about 8 times) between aspect angle contours during the first crossing than the second.

The measured aspect angle spread from approximately −3° to 3° as seen on Figure 3 (left) is therefore misleading. The spread is mainly due to a wide altitude-aspect angle radar ambiguity function. To demonstrate this point, we injected the best fit altitude profiles (shown in Figure 6) for the second crossing to simulate the echo reception for the first crossing. The results are shown in Figure 8. The aspect angle spread is over several degrees, despite the fact that the best fit aspect width profile is less than 0.5° at every altitude. Note that the simulation code computes the image between the altitudes of 80 and 130 km only. Despite altitudinal structure in the input profiles, the output here is shown as uniform in altitude. This is because the radar ambiguity function for the first crossing is very wide in altitude and therefore the *E* layer backscatter returns will overlap (or be integrated) at the receiver input. Just as the model predicts, the measured image on the LHS of Figure 3 shows no altitudinal structure.

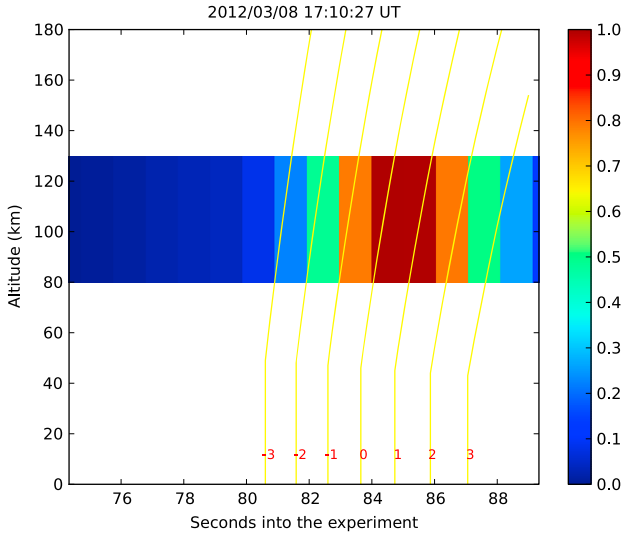

Figure 8. Simulation of scattering for the first crossing of EXPT1017, using as inputs the same altitude profiles (Figure 6) of aspect sensitivity for the second crossing. Although the input aspect sensitivities are < 0.5° at every altitude, the convolution of the radar beam with the radar ambiguity function shows scattering as much as 3°, in line with the measurement shown on Figure 3 (left). The intensity scale is linear. See text for details.

2.2. EXPT1018, 25 April 2012

Another backscattering event in conjunction with PFISR (EXPT1018) occurred on 25 April 2012 at 0254 UT. Figure 9 (similar to Figure 1) shows the spacecraft trajectory superimposed on the loci-of-perpendicularity. The *F* region $\mathbf{E} \times \mathbf{B}$ drift magnitude was ∼700 m/s and the direction was ∼53° north of geographic west. Note that the spacecraft is ascending in latitude. We calculated the flow angle of the waves that would produce backscatter as 124° for the first crossing and 31° for the second crossing.

Figure 10 shows the range-time-intensity plot for this event. Note the backscatter around 205 s immediately above direct pulse signal. This time coincides with the second crossing of the loci-of-perpendicularity for the altitude of 100 km. Interestingly, the RTI plot

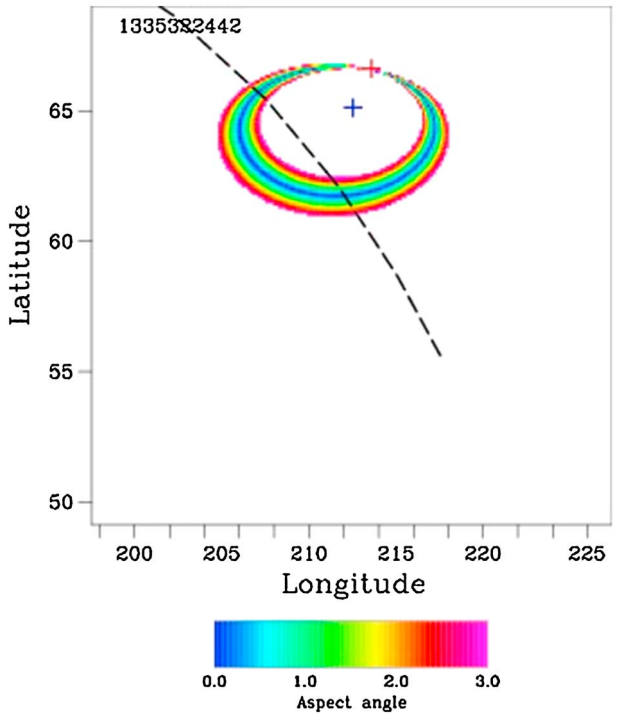

Figure 9. The loci-of-perpendicularity for the pass EXPT1018 for the altitude of 100 km. The spacecraft is ascending in latitude. The aspect angle scale is in degrees.

does not show backscatter from the first crossing, which would have happened around 85 s. We did not download the raw data for the first crossing due to data bandwidth limitations. However, it is possible that inspection of the raw data would have revealed backscatter. This was the case in EXPT1017 in which backscatter was not visible in the RTI, but backscatter was present in the raw data. However, since the instability is weakly driven, i.e., the $\mathbf{E} \times \mathbf{B}$ drift magnitude was only slightly above the ion acoustic threshold, and the flow angle for the first crossing was quite large, it is possible that the backscatter from the first crossing was too weak to detect.

The altitude-aspect angle mapping of the backscatter from the second crossing is shown in Figure 11. Note that the intensity scale is in dB. The range of backscattering altitudes is similar to those of EXPT1017, while the peak altitude is near 107 km. In contrast to the image for EXPT1017 (Figure 3, right), the aspect angle resolution was ~0.5°, about 4 times lower. Noticeably, there are only two data points between the contours. Again, as we discussed before, most of the data spread is due to the scattering geometry, i.e., the radar ambiguity function. Deconvolving the radar ambiguity function to 0.1° precision is much more difficult here. Regardless, one can visually estimate an aspect angle spread of <1° (more precisely, 4–5 dB drop in 0.5° on either side of the peak, or ~0.75° full width at 3 dB points). Considering the radar beam width contribution, this event also supports the conclusion from the EXPT1017 that the magnetic aspect sensitivity of FAI (RMS $\Delta\theta$) should be much less than 1° at the altitude of 110 km.

2.3. EXPT1019, 12 June 2012

The last natural irregularity backscattering event occurred in Resolute Bay, Canada, during an $\mathbf{E} \times \mathbf{B}$ drift of ~1000 m/s. The RTI plot is shown in Figure 12 (top). Figure 12 (bottom) shows a zoom to the echo. As seen from Figure 12 (top), the echoing occurred when the satellite was crossing the *E* region loci-of-perpendicularity. There is an earlier crossing of the loci-of-perpendicularity during the first 10 s of the plot. It is possible that there was echoing too; however, the echo is likely shadowed by the much stronger direct radar pulse because of the very short geometric delay between the echo and the direct pulse. Note that we did not apply the previous altitude-aspect angle analysis to EXPT1019 because the pulse length for this experiment was 480 μs, too long to resolve the *E* region.

Due to the brief and localized nature of the backscatter we have presented, we have considered the possibility of scatter from a meteor or spacecraft. However, we conclude that this is very unlikely. For the echoes

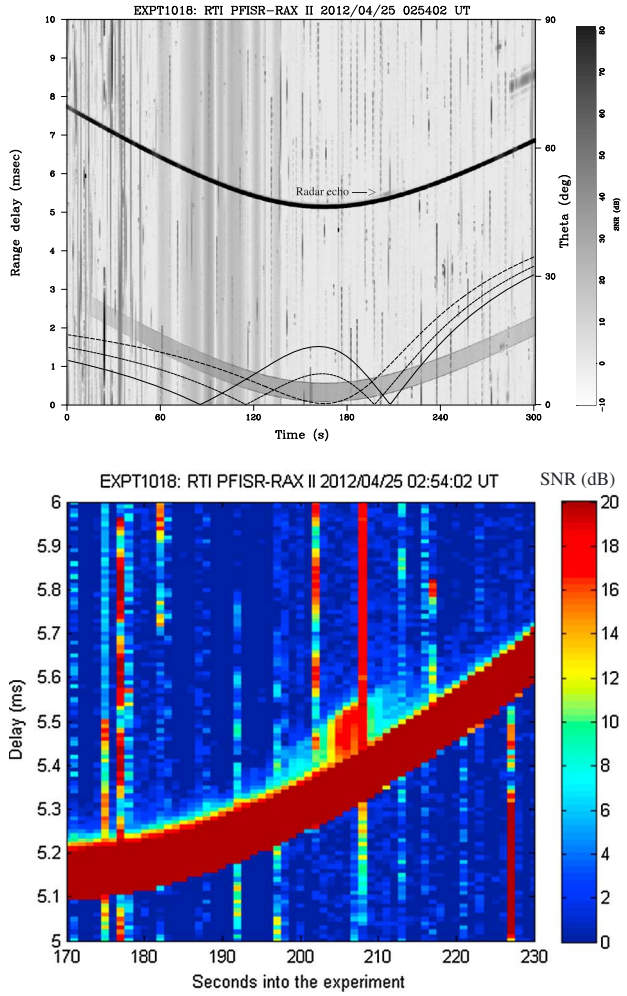

Figure 10. (top) Range-time-intensity plot for the pass EXPT1018 on 25 April 2012 at 0254 UT. The black trace is the 100 μs PFISR direct signal. The small gray region around 205 s arriving shortly after the direct signal is the *E* region echo. (bottom) A zoom into the echoing region.

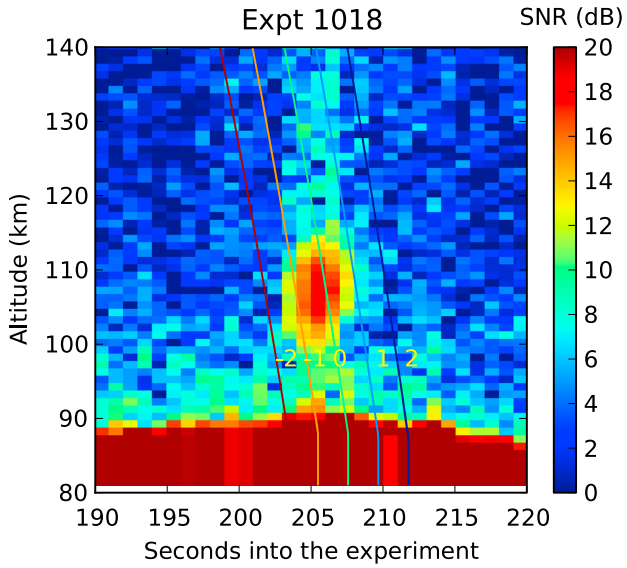

Figure 11. Altitude-aspect angle mapping of backscatter for EXPT1018, during which the *F* region ion drift was ∼700 m/s.

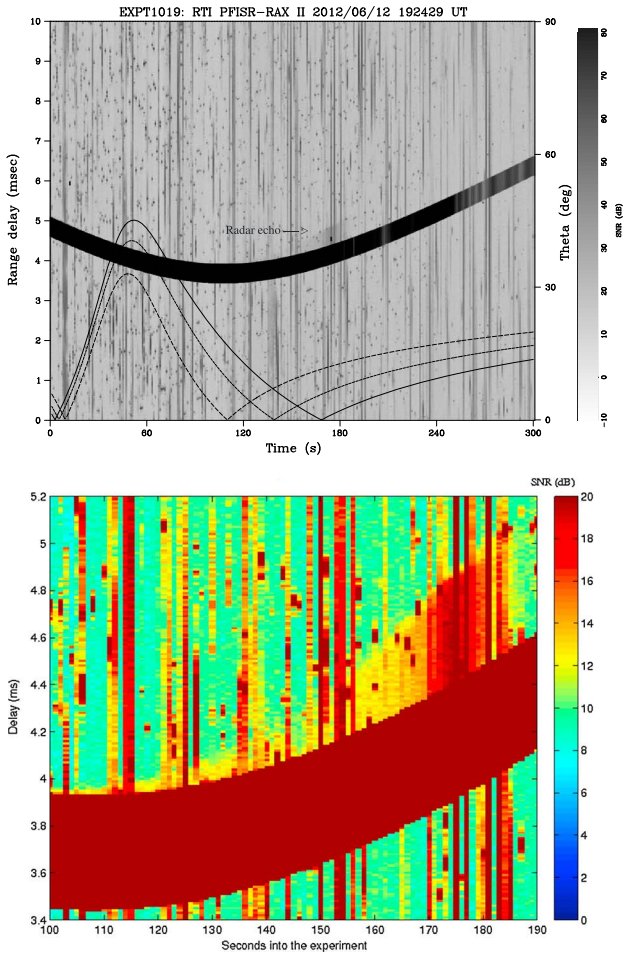

Figure 12. (top) Range-time-intensity plot for the pass EXPT1019 on 12 June 2012 at 1024 UT. The thick black trace is the 480 μs PFISR direct signal. Aspect angles corresponding to the irregularity altitudes of 100, 200, and 300 km are shown by the solid, short-dashed, and long-dashed red lines, respectively. Note that the ordinate for these lines is the right-hand *y* axis. FAI backscatter from those altitudes are expected when the aspect angle dips near zero. The shaded region around 175 s arriving shortly after the direct signal (black band) is the *E* region echo. (bottom) A zoom into the echoing region.

we presented here to be from a meteor or a spacecraft, the scattering event must occur at exactly 109 km or 330 μs delay and at the 228th second. Also, another scattering event must have occurred at the 84th second and at 20–30 μs delay, during the same pass. And two more scattering events must have occurred in the beam during EXPT1018 and EXPT1019 at exact times of crossings of loci-of-perpendicularity. Therefore, echoing from a meteor or spacecraft is an extremely unlikely explanation for the observation reported here.

3. Discussion

Our observational findings can be itemized as follows:

1. The echoes are observed only when the electron drift speed exceeds a threshold close to the ion acoustic speed C_s. We have run ~30 natural irregularity experiments and detected echoes only when the *F* region ion drift was ~700, ~1000, and ~1500 m/s, all exceeding the ion acoustic threshold (~500 m/s) for the Farley-Buneman instability. The ion drift speeds during the rest of the experiments as measured by the Poker Flat ISR or the Resolute Bay ISR were near or below 500 m/s. These threshold observations parallel those made in the comparisons of in situ sounding rocket electric field and ground-based imaging radar data during the two Joule campaigns in Alaska [*Bahcivan et al.*, 2005; *Hysell et al.*, 2008]. Although not discussed here, in a previous paper [*Bahcivan et al.*, 2012], we reported that the phase velocity obeys the empirical formula $C_s \cos\theta$.

2. To our knowledge, the profiles shown in Figure 5 provide the first altitudinally resolved estimates of magnetic aspect sensitivity of submeter-scale auroral irregularities. The backscatter is confined to the altitude range of 106–112 km (3 dB points), as seen on Figure 6 (left). The intensity at 100 km is almost 2 orders of magnitude smaller than the intensity at 110 km. Another experiment (EXPT1018), albeit with poorer resolution, shows a similar altitude distribution with a peak near 107 km.
3. The radar echoes are highly aspect-sensitive, with RMS aspect angles between 0.1° and 0.4° when descending in altitude from 110 km to 105 km. This aspect sensitivity range is also very similar to the range reported by *Kudeki and Farley* [1989] for equatorial *E* region irregularities. However, the RMS aspect angle at the peak of the scattering (109 km) is ~0.15°. Using this value, the power fall of 10 dB would occur within ~0.35°, which is significantly smaller than the values published by previous studies made at VHF and UHF [*Moorcroft and Schlegel*, 1990; *Foster et al.*, 1992; *Hall and Moorcroft*, 1992]. This difference is further contrasted by the fact that our measurements were made during a significantly large electric field (~80 mV/m), which should have produced larger RMS aspect angles, not smaller. Note that previous studies were not height-resolved and therefore do not single out a specific altitude. However, if we used the upper end of the aspect sensitivity profile at 0.4°, which corresponds to the altitude of 105 km and lower, we would observe a power fall of 13 dB at 1° away from perpendicularity. This value is in reasonable agreement with previous studies.
4. The aspect angle distribution does not favor $\pm \sim 0.5°$ as predicted by the linear theory [*Fejer et al.*, 1984]. In fact, it is single-peaked and the mean aspect angle (θ_m) varies between 0.4° at 105 km to 0.0° at 115 km. A rough estimate shows that if a thin sheet of electrojet Hall current generates 550 nT perturbation on the ground (which is the value recorded by the Poker Flat magnetometer during the experiment), the magnetic field immediately above and below this current will be bent by 550 nT as well. Considering ~50,000 nT total geomagnetic field, the resulting perturbation will bend the field by $\pm \sim 0.5°$ above and below the sheet. Therefore, the variation in the background magnetic field direction could be on the order of the magnetic aspect angle bias (0–0.4°) we report here.

Below, we further discuss our second and third findings. The significant (20 dB) drop of backscatter power from 110 km to 100 km is unexpected because rocket-based in situ electric field measurements representing meter-scale irregularities [*Pfaff et al.*, 1984; *Rose*, 1992] do not show such drop. For example, Figure 2c in *Pfaff et al.* [1984] shows turbulent electric field fluctuations as a function of altitude. The signal is filtered at 50–1000 Hz to select high-frequency oscillations corresponding to meter-scale waves. The ratios of the intensities at the altitudes of 110 and 100 km is about two thirds; that is, the intensity at 100 km is actually higher.

We have considered whether the 20 dB power drop we observe is because of the background N_e (assuming that the backscatter power is proportional to N_e, which is true if the instability saturates at a fixed percentage density fluctuation). Figure 13 shows raw power and fitted N_e estimates from PFISR based on the 100 μs and the 480 μs pulses. These PFISR measurements do not have the resolution to resolve the *E* region at km scales. Nevertheless, a rough linear fit shows that the N_e increase around 100 km is about 3 dB per 10 km, too small to explain the 20 dB drop.

The magnetic field alignment within 0.1–0.2° for the altitude of 110 km at ~80 mV/m electric field is significantly narrower than expected. Even considering that the RMS of perpendicular wave electric fields is on the order of the background electric field (80 mV/m), the corresponding $E_{||}$ will be between 0.13 and 0.27 mV/m. Electron plasma heating models [*Milikh and Dimant*, 2003b; *Bahcivan et al.*, 2006] show that ~1 mV/m $\delta E_{||}$ is needed to heat the electrons to the observed temperatures of ~1500 K at the altitude of 110 km and for an electric field of 80 mV/m. The fully kinetic 3-D simulation study by *Oppenheim and Dimant* [2013] is the most recent theoretical work on the wave heating of *E* region electrons. For a strongly driven case (~2000 m/s electron drift), the simulations for the altitude of 112 km yield $\sqrt{\langle E_{||}^2 \rangle / \langle E_{\perp}^2 \rangle} \approx 0.0275$ corresponding to $\approx 1.6°$ aspect angle spread. This is an order of magnitude larger than what we report here ($\sim 0.15°$).

Therefore, to the extent that our measurements from a single event here are representative of submeter scales at the altitude of 110 km, submeter waves have too small $\delta E_{||}$ to contribute to electron heating. It is possible that submeter waves at larger aspect angles are more heavily dissipated. It is also possible that our measurements at an $\mathbf{E} \times \mathbf{B}$ flow angle of 55° reflect the properties of secondary waves only and that primary submeter waves may propagate at larger aspect angles. Moreover, it could be that the dominant

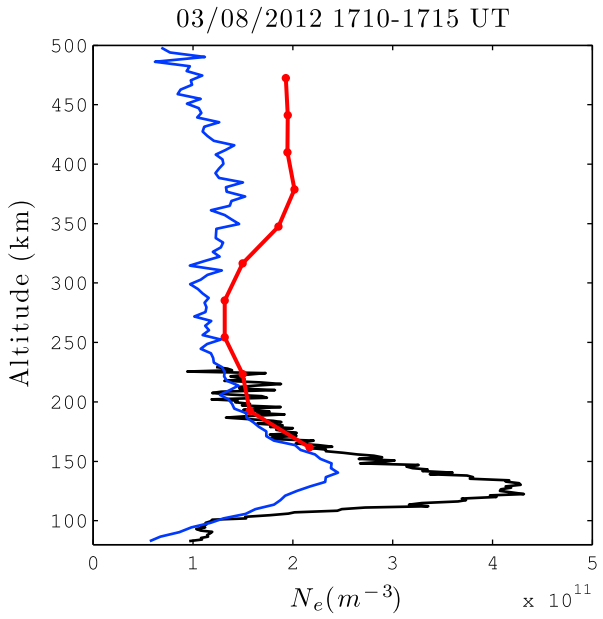

Figure 13. Electron density (N_e) estimates from PFISR diagnostic pulses during EXPT1017. Fitted N_e (red line) and raw N_e (blue line) from the 480 μs pulses, and raw N_e from the 100 μs pulse scaled to match the fitted N_e at ~200 km (black line).

wave heating is caused by larger scale waves. As the simulations of *Oppenheim and Dimant* [2013] predict, the dominant wave energy starts at meter-scale but then progresses to longer wavelengths, not shorter.

A direct comparison of our aspect sensitivity measurements here to the results from previous ground-based radar studies is not possible because of the large differences in the resolutions. In particular, these studies are studying aspect sensitivity indirectly, by trying to measure the power drop as they scan away from perpendicularity. However, the spatial extent of the beam width at the point of scattering is too wide to resolve the backscatter in aspect angle or in altitude. For example, for the European Incoherent Scatter (EISCAT) system, at a radar range of 400 km and at an elevation of 15°, two *E* region altitudes separated by only 7 km (which is about the width of the altitude range of echoes we observed) would appear more than a degree apart in the loci-of-perpendicularity. For this reason, previous studies mostly reported aspect angle distributions with a coarseness of 1° or higher [*Moorcroft and Schlegel*, 1990; *Foster et al.*, 1992; *Hall and Moorcroft*, 1992]. Moreover, ground-based radars have the dynamic range and sufficient statistics to measure the aspect angles at larger angles from perpendicularity. For example, *Jackel et al.* [1997] and *Schlegel and Moorcroft* [1989], using EISCAT, measured aspect sensitivity at magnetic aspect angles between 5° and 11°) and *Moorcroft* [1996], using the Prince Albert Radar, between 4.5° and 16°. RAX-2 measurements presented here have limited dynamic range (<20 dB) and can show the power drop only within the first degree, with no sensitivity for higher degrees.

Hereinafter, we discuss a possible explanation for wave propagation at very small (~0.1°) aspect angles. Note that many of the observations we have reported above match the characteristics of Farley-Buneman waves very well, notably the altitude of occurrence, the phase speed, the threshold $\mathbf{E} \times \mathbf{B}$ drift for excitation, and the strong alignment with the magnetic field. However, the measured wave propagation at aspect angles even smaller than that predicted by the linear theory is puzzling.

Excluding plasma recombination, in the absence of plasma density gradients, and in the frame of ions, the frequency and growth rate expressions derived by *Fejer et al.* [1975] for the linear stage of the instability reduce to

$$\omega = \frac{\mathbf{k} \cdot \mathbf{V}_{\mathrm{de}}}{1 + \psi} \tag{1}$$

$$\gamma = \frac{1}{1 + \psi} \left[\frac{\psi}{\nu_i} \{ \omega^2 - k^2 C_s^2 \} \right] \tag{2}$$

where

$$\psi = \frac{\nu_e \nu_i}{\Omega_e \Omega_i} \left(1 + \frac{\Omega_e^2}{\nu_e^2} \frac{k_\parallel^2}{k_\perp^2} \right). \tag{3}$$

In the above equations, $\mathbf{V}_{\mathrm{de}}$ and $\mathbf{V}_{\mathrm{di}}$ are the electron and ion drift velocities, Ω and ν refer to gyro and collision frequencies (with neutrals) for the ions and electrons, and ψ is the so-called anisotropy factor, which depends on the magnetic aspect angle. The C_s term is the ion acoustic speed, which may be expressed as

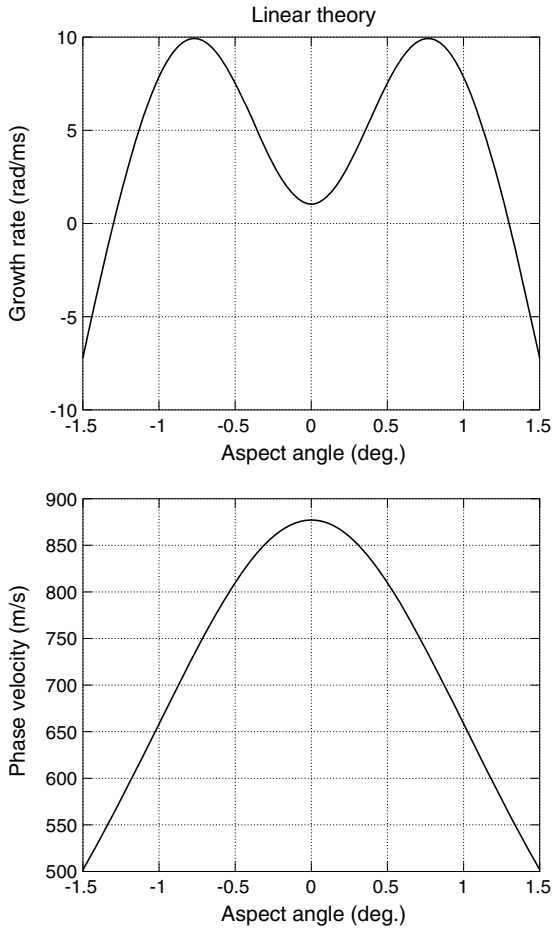

Figure 14. (top) Phase velocity and (bottom) growth rate for a 0.55 m Farley-Buneman wave driven by a 1543 m/s $\mathbf{E} \times \mathbf{B}$ drift at a flow angle of 55°.

$C_s^2 = K_B(\gamma_e T_e + \gamma_i T_i)/m_i$. The symbol γ used here now refers to ratios of specific heats which vary slightly with altitude according to kinetic theory [*Farley*, 1963].

Figure 14 shows the phase velocity (top) and growth rate (bottom) as a function of aspect angle for a 0.55 m wave propagating at an altitude of 110 km and at an angle of 55° from the main $\mathbf{E} \times \mathbf{B}$ flow direction. The wave is driven by an $\mathbf{E} \times \mathbf{B}$ drift of 1543 m/s in a plasma with the following parameters representing the $\mathbf{E} \times \mathbf{B}$ drift and plasma conditions during EXPT1017: $C_s = 562$ m/s, flow s^{-1}, $\nu_e = 25000\ s^{-1}$, and $B = 0.5$ G. The C_s value is empirically set based on the formula of *Nielsen and Schlegel* [1985]. As reported in *Bahcivan et al.* [2012], that empirical value and the $C_s \cos\theta$ expression matched the measured phase speed (300–400 m/s) within the uncertainty of a wind-driven ion drift. Figure 14 shows that the growth rate maximizes around ±0.75°. In the linear regime, if an unstable wave propagates in a range of aspect angles for which the growth rate is positive, then we should have measured an aspect angle distribution between −1.3° and +1.3°, with the double peaks located at ±0.75°. As the waves grow toward the nonlinear stage, we expect that the region between the peaks will fill up through mode coupling and additional waves will be generated at aspect angles beyond 1.3°. We, therefore, expect an aspect angle distribution with an RMS width no less then 1°. However, our measurements are indicating a very narrow aspect angle distribution centered at perpendicularity, even narrower than the distribution of a marginally unstable wave (linear wave). This is the most puzzling aspect of the observation.

One possibility is that the dominant scattering is from secondary waves generated by the mode coupling of two or more primary waves, and that the scattering from linearly unstable waves is buried under this dominant scattering. A narrow aspect angle distribution would occur if the following two conditions are met: (1) mode coupling of two wave vectors in the primary direction (near $\mathbf{E} \times \mathbf{B}$ flow) produces secondary modes that are decaying at a rate that depends on their aspect angle and (2) the secondary waves with

exact perpendicularity have the longest decay time, while those secondary waves with some angles off perpendicularity decay much faster.

At this point, we heuristically invoke the growth rate expression in equation (2), although the expression is valid only for the linear stage of the instability. The heuristic assumption is that those waves with phase velocity greater than C_s grow and those lower than C_s decay. Note also that among the decaying waves, the ones with larger aspect angles decay fast (because their growth rate is more negative), while those propagating at near perpendicularity prevail for a long time (growth rate is less negative). It is therefore possible that we are scattering from these prevailing waves. In other words, secondary waves propagating at exact perpendicularity to the magnetic field are acting as fossils of plasma turbulence (due to their long decay time) intensely generated by primary waves whose phase velocity is slightly above C_s. Investigating this mechanism will require extensive new modeling investigations.

4. Conclusion

We have used, for the first time, a ground-to-space bistatic radar scattering geometry to obtain height-resolved measurements of radar aurora at subdegree magnetic aspect angle resolution. To our knowledge, these measurements have the highest combined altitude-aspect angle resolutions thus far. A small set of RAX-2 conjunctions with PFISR resulted in detection of *E* region coherent backscatter, which is then used to obtain aspect sensitivity of submeter scale irregularities. Based on a set of compelling events, we show that the magnetic aspect sensitivity of submeter scale irregularities is much higher than previously reported. This suggests that submeter scale waves have too small parallel electric fields to contribute significantly to *E* region electron heating.

It must be noted that the measurements were made at large flow angles and that submeter waves propagating very close to the $\mathbf{E} \times \mathbf{B}$ flow may propagate at larger aspect angles. Due to a limited set of measurements, we could not verify this, and further measurements with RAX-2 are not possible since it is no longer operational. It is also possible that the submeter scale regime is subject to larger dissipative effects than the meter-scales. The effective bistatic Bragg wavelength of 0.53 m is comparable to the collisional mean free path of ions and, therefore, ion Landau damping could be playing a substantial role for submeter waves at 110 km [*Dimant and Sudan*, 1995]. In this regard, electron heating models that rely on parallel electric fields associated with meter-scale or longer wavelength turbulence [*Milikh and Dimant*, 2003a, 2003b; *Bahcivan et al.*, 2006; *Oppenheim et al.*, 2008; *Oppenheim and Dimant*, 2013] would still operate. However, the transition from submeter scales to meter scales needs to be better explored.

It is possible that the dynamics of decameter or longer wavelengths significantly contribute to anomalous electron heating in the auroral electrojet. In particular, *Oppenheim and Dimant* [2013] reported that in the saturated turbulence state, the most energetic modes are the longest ones allowed in the system (> 30 m). In addition, *Bahcivan and Cosgrove* [2010] proposed that parallel electric fields associated with long wavelength waves in the presence of vertical electron density gradients ∇n_e would be sufficient to heat the electrons. Moreover, *Haldoupis et al.* [2000] showed that kilometric-scale vertical ∇n_e are statistically linked to strong electric field conditions. Therefore, when we observe enhanced *E* region electron temperatures, the necessary conditions are also present for the generation of long wavelength waves propagating at large aspect angles.

Appendix A : The Deconvolution Algorithm

The altitude profiles shown in Figure 6 are obtained by solving the minimization problem

$$\min_{\mathbf{x}\in R^n} \{A(f(\mathbf{x}), \mathbf{y}) + \gamma B(\mathbf{x})\} \tag{A1}$$

where $\mathbf{x} = (\mathbf{I}, \Delta\theta, \theta_\mathbf{m})$ is composed of altitude profiles of intensity $\mathbf{I}$, aspect width $\Delta\theta$ and mean aspect angle θ_m, for the altitude range of 81–130 km, with 1 km increments. Therefore, $n = 150$. The function f is the forward model of scattering. For a given $\mathbf{x}$, it computes an aspect angle-time intensity image, e.g., Figure 3, that would be measured by the spacecraft. The vector $\mathbf{y}$ contains the measurements, i.e., the pixels

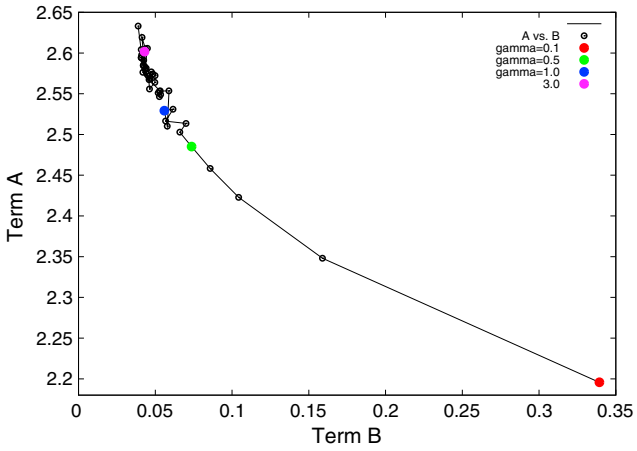

Figure A1. The covariation of the terms A and B as the smoothness control parameter γ is varied.

of the altitude-time intensity images. For the second crossing of EXPT1017, the image has the dimensions of 50 pixels in the altitude direction and 40 pixels in the time direction. Therefore, we fit for a total of $M = 2000$ data points. The function A computes the weighted mean of the squares of the model and measurement differences as follows:

$$A(f(\mathbf{x}), \mathbf{y}) = \frac{1}{M} \sum_{ij} \frac{[f_{ij}(x) - y_{ij}]^2}{\sigma_{ij}^2} \tag{A2}$$

where the indices ij denote the pixel position corresponding to the ith altitude and jth time. The measurement uncertainties, σ_{ij}, are computed as follows:

$$\sigma_{ij} = \frac{p_{ij} - n_0}{\sqrt{N}} \left(1 + \frac{1}{(p_{ij} - n_0)/n_0}\right), \tag{A3}$$

where p_{ij} is the backscatter intensity measured at the pixel ij and n_0 is the noise power, which can be estimated from the image regions where no backscatter is noticeable, i.e., blue regions. N is the number of incoherently averaged radar samples; $N = 100$ for EXPT1017. The σ_{ij} expression above is valid only if the radar signal is composed of Gaussian noise and auroral backscatter only. However, we suspect that considerable amount of interference is modulating the apparent noise floor. We, therefore, bounded σ_{ij} by an empirical minimum given by the intensity variances in the image regions where no visible backscatter is present.

The function B computes an inverse measure of smoothness as follows:

$$B(\mathbf{x}) = \sum_k \alpha_1 \left| \frac{\partial I_k^2}{\partial h_k^2} \right|^2 + \alpha_2 \left| \frac{\partial \Delta\theta_k^2}{\partial h_k^2} \right|^2 + \alpha_3 \left| \frac{\partial \theta_{m,k}^2}{\partial h_k^2} \right|^2 \tag{A4}$$

where $k = 1 : n$. The weighting of the three terms on the RHS are all set to 1 for simplicity. Note that $\Delta\theta[h]$ and $\theta_m[h]$ profiles are handled in degrees and the peak of the intensity profile $I[h]$ is normalized, so all the profiles are given in comparable fractions of 1.

The parameter γ in equation (A1) controls the relative contribution of the regularization term and the resulting fits. Figure A1 shows the relative contribution of A and B for a range of γ. The red point at the lower-right corner corresponds to $\gamma = 0.1$. The solution for this case is shown at Figure A2 (top). For the rest of Figure A1, the solutions correspond to the green, blue, and magenta points. As γ is increased, the solution is smoother, i.e., with less artifacts. The solution presented in the discussion is that of the case $\gamma = 1.0$. We find that in the altitude region where the intensity is highest, 106–112 km, there is little sensitivity to the γ. We can be confident that the regularization is not biasing the fits in this region.

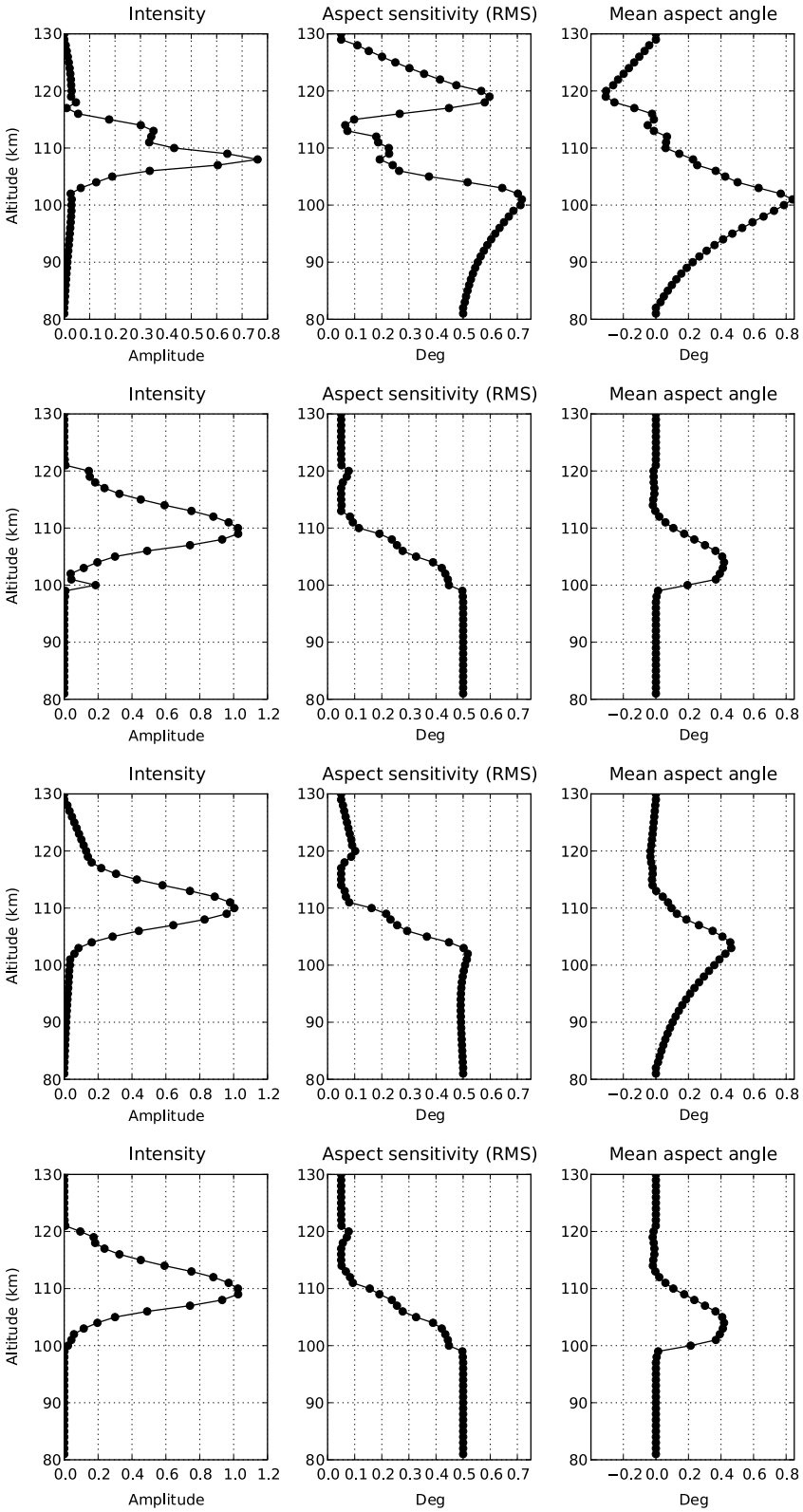

Figure A2. Altitude profile fits for $\gamma = 0.1$, 0.5, 1.0, and 3.0, from top to bottom, respectively. Both the (top) "noisy" solution and (bottom) the smoothest solution agree the most between the altitudes of 106 and 112 km, where the backscatter signal is present.

Acknowledgments
RAX-2 was developed under National Science Foundation (NSF) grant ATM-0121483 to SRI International and the University of Michigan. Some of the analysis was carried out under NSF ATM-1139151 to SRI. Additional support is provided by the Department of Defense through a National Defense Science and Engineering Graduate (NDSEG) Fellowship to the third author. The Poker Flat Incoherent Scatter Radar is operated by SRI International on behalf of the National Science Foundation under NSF Cooperative Agreement ATM-0608577. We greatly appreciate comments and suggestions from the three reviewers and from Roland Tsunoda and Russell Cosgrove in improving this paper.

Robert Lysak thanks Meers Oppenheim and an anonymous reviewer for their assistance in evaluating this paper.

References

Bahcivan, H. (2007), Plasma wave heating during extreme electric fields in the high-latitude *E* region, *Geophys. Res. Lett.*, *34*, L15106, doi:10.1029/2006GL029236.

Bahcivan, H., and R. Cosgrove (2010), On the generation of large wave parallel electric fields responsible for electron heating in the high-latitude *E* region, *J. Geophys. Res.*, *115*, A10304, doi:10.1029/2010JA015424.

Bahcivan, H., and J. Cutler (2012), Radio aurora explorer: Mission science and radar system, *Radio Sci.*, *47*, RS2012, doi:10.1029/2011RS004817.

Bahcivan, H., D. L. Hysell, M. F. Larsen, and R. F. Pfaff (2005), The 30 MHz imaging radar observations of auroral irregularities during the JOULE campaign, *J. Geophys. Res.*, *110*, A05307, doi:10.1029/2004JA010975.

Bahcivan, H., R. Cosgrove, and R. Tsunoda (2006), Parallel electron streaming in the high-latitude *E* region and its effect on the incoherent scatter spectrum, *J. Geophys. Res.*, *111*, A07306, doi:10.1029/2005JA011595.

Bahcivan, H., M. C. Kelley, and J. W. Cutler (2009), Radar and rocket comparison of UHF radar scattering from auroral electrojet irregularities: Implications for a nanosatellite radar, *J. Geophys. Res.*, *114*, A06309, doi:10.1029/2009JA014132.

Bahcivan, H., J. W. Cutler, M. Bennett, B. Kempke, J. C. Springmann, J. Buonocore, M. Nicolls, and R. Doe (2012), First measurements of radar coherent scatter by the Radio Aurora Explorer CubeSat, *Geophys. Res. Lett.*, *39*, L14101, doi:10.1029/2012GL052249.

Buneman, O. (1963), Excitation of field aligned sound waves by electron streams, *Phys. Rev. Lett.*, *10*, 285–287.

Dimant, Y. S., and M. M. Oppenheim (2011a), Magnetosphere-ionosphere coupling through *E* region turbulence: 1. Energy budget, *J. Geophys. Res.*, *116*, A09303, doi:10.1029/2011JA016648.

Dimant, Y. S., and M. M. Oppenheim (2011b), Magnetosphere-ionosphere coupling through *E* region turbulence: 2. Anomalous conductivities and frictional heating, *J. Geophys. Res.*, *116*, A09304, doi:10.1029/2011JA016649.

Dimant, Y. S., and R. N. Sudan (1995), Kinetic theory of the Farley-Buneman instability in the *E* region of the ionosphere, *J. Geophys. Res.*, *100*(8), 14,605–14,623.

Farley, D. T. (1963), A plasma instability resulting in field-aligned irregularities in the ionosphere, *J. Geophys. Res.*, *68*, 6083–6097.

Fejer, B. G., D. T. Farley, B. B. Balsley, and R. F. Woodman (1975), Vertical structure of the VHF backscattering region in the equatorial electrojet and the gradient drift instability, *J. Geophys. Res.*, *80*, 1313–1324, doi:10.1029/JA080i010p01313.

Fejer, B. G., J. F. Providakes, and D. T. Farley (1984), Theory of plasma waves in the auroral *E* region, *J. Geophys. Res.*, *89*, 7487–7494.

Foster, J. C., and P. J. Erickson (2000), Simultaneous observations of *E* region coherent backscatter and electric field amplitude at *F* region heights with the Millstone Hill UHF radar, *Geophys. Res. Lett.*, *27*(19), 3177–3180.

Foster, J. C., D. Tetenbaum, C. F. d. Pozo, J. P. St-Maurice, and D. R. Moorcroft (1992), Aspect angle variations in intensity, phase velocity and altitude for high-latitude 34 cm *E* region irregularities, *J. Geophys. Res.*, *97*, 8601–8617.

Haldoupis, C., K. Schlegel, and G. Hussey (2000), Auroral *E* region electron density gradients measured with EISCAT, *Ann. Geophys.*, *18*, 1172–1181.

Hall, G. E., and D. R. Moorcroft (1992), Magnetic aspect angle effects in radar aurora at 48.5 MHz, corrected for refraction, *J. Geophys. Res.*, *97*(A12), 19,471–19,488.

Hysell, D. L., G. Michhue, M. F. Larsen, R. Pfaff, M. Nicolls, C. Heinselman, and H. Bahcivan (2008), Imaging radar observations of Farley Buneman waves during the JOULE II experiment, *Ann. Geophys.*, *26*, 1837–1850.

Jackel, B. J., D. R. Moorcroft, and K. Schlegel (1997), Characteristics of very large aspect angle *E* region coherent echoes at 933 MHz, *Ann. Geophys.*, *15*(A7), 54–62.

Kudeki, E., and D. T. Farley (1989), Aspect sensitivity of equatorial electrojet irregularities and theoretical implications, *J. Geophys. Res.*, *94*, 426–434.

Milikh, G. M., and Y. S. Dimant (2003a), Model of anomalous electron heating in the *E* region: 1. Basic theory, *J. Geophys. Res.*, *108*(A9), 1350, doi:10.1029/2002JA009524.

Milikh, G. M., and Y. S. Dimant (2003b), Model of anomalous electron heating in the *E* region: 2. Detailed numerical modeling, *J. Geophys. Res.*, *108*(9), 1351, doi:10.1029/2002JA009527.

Moorcroft, D. R., and K. Schlegel (1990), Height and aspect sensitivity of large aspect angle coherent backscatter at 933 MHz, *J. Geophys. Res.*, *95*, 19,011–19,021.

Moorcroft, D. R. (1996), A statistical study of UHF auroral backscatter at large magnetic aspect angle: A reanalysis of unpublished results from 1068, *J. Geophys. Res.*, *107*, 1301.

Moretto, T. (2008), CubeSat mission to investigate ionospheric irregularities, *Space Weather*, *6*, S11002, doi:10.1029/2008SW000441.

Nielsen, E., and K. Schlegel (1985), Coherent radar Doppler measurements and their relationship to the ionospheric electron drift velocity, *J. Geophys. Res.*, *90*, 3498–3504.

Oppenheim, M. M., and Y. S. Dimant (2013), Kinetic simulations of 3-D Farley-Buneman turbulence and anomalous electron heating, *J. Geophys. Res. Space Physics*, *118*, 1306–1318, doi:10.1002/jgra.50196.

Oppenheim, M. M., Y. S. Dimant, and L. P. Dyrud (2008), Large-scale simulations of 2-D fully kinetic Farley-Buneman turbulence, *Ann. Geophys.*, *26*, 543–553.

Pfaff, R. F., M. C. Kelley, B. G. Fejer, E. Kudeki, C. W. Carlson, A. Pedersen, and B. Hausler (1984), Electric field and plasma density measurements in the auroral electrojet, *J. Geophys. Res.*, *89*(A1), 236–244.

Rose, G. (1992), Three-component AC E-field observations during the rocket and scatter experiment in 1988–1989 under radar auroral conditions in northern Scandinavia, *J. Atmos. Terr. Phys.*, *54*(6), 669–679.

Schlegel, K., and D. R. Moorcroft (1989), EISCAT as a tristatic auroral radar, *J. Geophys. Res.*, *94*(A2), 1430–1438.

Schlegel, K., and J. P. St.-Maurice (1981), Anomalous heating of the polar *E* region by unstable plasma waves: 1. Observations, *J. Geophys. Res.*, *86*, 1447–1452.

St.-Maurice, J. P., K. Schlegel, and P. M. Banks (1981), Anomalous heating of the polar *E* region by unstable plasma waves 2. Theory, *J. Geophys. Res.*, *86*, 1453–1462.

Tsunoda, R. T., R. I. Presnell, and R. L. Leadabrand (1974), Radar auroral echo characteristics as seen by a 398-MHz phased array radar operated at Homer, Alaska, *J. Geophys. Res.*, *79*, 4709–4724.